ATLAS NOTE

ATLAS-CONF-2011-024

March 13, 2011

Search for neutral MSSM Higgs bosons decaying to $\tau^+\tau^-$ pairs in proton-proton collisions at $\sqrt{s}$ = 7 TeV with the ATLAS Experiment

The ATLAS Collaboration

Abstract

A search for neutral Higgs bosons A, H, h in the Minimal Supersymmetric Standard Model with the ATLAS detector at the LHC is presented. The analysis is based on proton-proton collisions at a center-of-mass energy of 7 TeV, corresponding to an integrated luminosity of 36 pb^{-1}, and focuses on Higgs decays into two τ leptons, $A/H/h \to \tau^+\tau^-$, where one τ lepton decays leptonically and the other hadronically. After signal selection, 206 events are observed in this data sample. The observed number of events is consistent with the total background estimate of 195 ± 33 events, where the most important background contributions are obtained from data control samples. A 95% confidence-level exclusion limit for MSSM $A/H/h$ production is derived as a function of the parameters m_A and $\tan\beta$.

1 Introduction

Discovering the mechanism responsible for electroweak symmetry breaking and the origin of mass for elementary particles [1, 2, 3, 4] is one of the major goals of the physics program at the Large Hadron Collider (LHC) [5]. In the Standard Model this mechanism requires the existence of a scalar particle, the Higgs boson. Extending the Standard Model to the Minimal Supersymmetric Standard Model (MSSM), two Higgs doublets of opposite hypercharge are required, resulting in five observable Higgs bosons. Three of these Higgs bosons are electrically neutral (h, H, and A) while two are charged ($H^{\pm}$). At tree level and in the absence of CP-violating phases their properties such as masses, widths, and branching ratios can be predicted in terms of only two parameters, often chosen to be the mass of the CP-odd Higgs boson, m_A, and the ratio of the vacuum expectation values of the two Higgs doublets, $\tan\beta$.

In the MSSM, the couplings of the Higgs bosons to fermions and bosons are different from those in the Standard Model, resulting in different production cross sections and decay rates. While decays into ZZ or WW are dominant in the Standard Model for Higgs boson masses above ~ 140 GeV, in the MSSM these decay modes are either suppressed by $\cos(\beta - \alpha)$ for the H boson, where α is the mixing angle of the two CP-even Higgs bosons, or even absent for the A boson. However, the coupling of the Higgs boson to third-generation fermions is strongly enhanced for large regions of the MSSM parameter space. The decay of the neutral Higgs bosons into a pair of τ leptons is one of the most promising channels for Higgs-boson searches at the LHC. In the MSSM, the Higgs-boson production can proceed via gluon fusion or in association with b quarks. In particular the latter becomes more important for large values of $\tan\beta$. Searches for MSSM Higgs bosons have been performed at LEP [6] and the Tevatron [7].

In this note, a search for neutral MSSM Higgs bosons in the decay mode $A/H/h \to \tau^+\tau^-$ with the ATLAS experiment at CERN is presented. The analyzed data were recorded in proton-proton collisions at a center-of-mass energy of 7 TeV at the LHC up to the end of 2010. The data sample corresponds to an integrated luminosity of (36.1 ± 1.2) pb^{-1} [8].

For the $A/H/h \to \tau^+\tau^-$ decays only final states with a charged light lepton (electron or muon) from a leptonic τ decay ($\tau^- \to e^-/\mu^-\bar{\nu}_{e/\mu}\nu_\tau$) and a hadronic decay of the other τ lepton are considered ("lepton-hadron channel"). This decay channel of the $\tau^+\tau^-$ pair has a branching ratio of 46%.

Methods to estimate the contributions of the most important background processes from control regions in data have been developed. An exclusion limit on $A/H/h$ production is set in the $m_h^{\max}$ scenario [9] as a function of m_A and $\tan\beta$.

2 The ATLAS Detector

The ATLAS detector is described in detail elsewhere [10]. The inner tracking detector is immersed in a 2-Tesla magnetic field provided by a superconducting solenoid. Charged-particle tracking measurements are made by silicon pixel and microstrip detectors in the pseudorapidity range $|\eta| < 2.5$ and by a straw-tube tracking chamber in the range $|\eta| < 2.0$ which enhances electron identification by the detection of transition-radiation photons. The calorimeters instrument the range $|\eta| < 4.9$, using a variety of detector technologies. The lead-liquid argon (LAr) electromagnetic calorimeter is divided into a barrel component ($|\eta| < 1.475$) and two endcap components ($1.375 < |\eta| < 3.2$). The hadronic tile calorimeter is placed directly outside the barrel electromagnetic calorimeter envelope. This steel-scintillating tile detector consists of a barrel covering the region $|\eta| < 1.0$ and two extended barrels in the range $0.8 < |\eta| < 1.7$. The copper-LAr hadronic endcap calorimeter consists of two independent wheels per endcap ($1.5 < |\eta| < 3.2$) located directly behind the endcap electromagnetic calorimeter. Larger values of $|\eta|$ (up to $|\eta| < 4.9$) are covered by the forward calorimeters which consist of three modules in each endcap: the first made of copper-LAr is optimized for electromagnetic measurements while the other two made of tungsten-LAr measure primarily the energy of hadronic interactions. The muon spectrometer measures the deflection

of muon tracks in the field of three large superconducting air-core toroid magnets. It is instrumented with separate trigger and high-precision tracking chambers. The trigger is provided by resistive plate chambers in the barrel ($|\eta| < 1.05$) and thin gap chambers in the endcap regions (up to $|\eta| < 2.4$). Over most of the pseudorapidity range, precision measurements in the principal bending direction are made with monitored drift tubes. The range $2.0 < |\eta| < 2.7$ of the innermost of the three layers is covered by higher granularity cathode strip chambers.

3 Signal and background processes and data samples

3.1 Higgs boson production

In the MSSM, Higgs bosons are produced via gluon-fusion, which is dominant for low Higgs boson masses and small values of $\tan\beta$, or in association with b quarks. The cross sections for Higgs boson production have been calculated using HIGLU [11] and ggh@nnlo [12] for gluon-fusion process. For the cross section of the $b\bar{b}A/H/h$ process the four-flavor scheme [13, 14] is used. The masses, couplings and branching ratios of the Higgs bosons have been computed with FeynHiggs [15]. Details of the calculations and associated scale, α_S and PDF uncertainties can be found in Ref. [13].

The direct $gg \to A/H/h$ production via gluon fusion was simulated with MC@NLO [16] and the associated $b\bar{b}A/H/h$ production with SHERPA [17]. The pseudoscalar A-boson samples for both production processes are generated for 11 masses m_A in the range from 90 to 300 GeV and $\tan\beta = 20$. These samples are also employed for H and h assuming the m_h^{max} MSSM benchmark scenario [9] and the same kinematics for the decay products. The signal sample with m_A closest to the computed mass of the H and h are used for H and h production, respectively. For other $\tan\beta$ values the simulated samples for $\tan\beta = 20$ are used and the cross section is scaled according to the cross-section ratio. The increase of the Higgs-boson natural width with $\tan\beta$ is neglected compared to the experimental mass resolution. Table 1 shows the values of cross section times branching ratio for selected values of m_A.

Table 1: Cross sections (multiplied by the relevant branching ratios (BR)) used in this note; NNLO calculation for W/Z+jets and $b\bar{b}A/H/h \to \tau^+\tau^-$, NLO+NNLL for $t\bar{t}$, NLO for single-t and di-boson production (MC@NLO samples), NNLO for $gg \to WW$ (gg2WW samples) and NNLO (top loop)+NLO (bottom loop and top/bottom-loop interference) for direct $gg \to A/H/h \to \tau^+\tau^-$. The signal cross sections are given for $\tan\beta = 20$ and the three values correspond to $A/H/h$ production.

Process	Cross section × BR [pb]
$bbA/H/h$, $A/H/h \to \tau^+\tau^- \to \ell\tau_h$, $m_A = 120$ GeV	3.57/0.33/3.43
$bbA/H/h$, $A/H/h \to \tau^+\tau^- \to \ell\tau_h$, $m_A = 200$ GeV	0.56/0.56/0.03
$gg \to A/H/h \to \tau^+\tau^- \to \ell\tau_h$, $m_A = 120$ GeV	2.25/1.01/1.87
$gg \to A/H/h \to \tau^+\tau^- \to \ell\tau_h$, $m_A = 200$ GeV	0.14/0.17/0.50
$W \to \ell$+jets ($\ell = e, \mu, \tau$)	10.46×10^3
$Z/\gamma^* \to \ell^+\ell^-$+jets ($m_{\ell\ell} > 10$ GeV)	4.96×10^3
$t\bar{t}$	164.6
Single-t ($t-$, $s-$ and Wt-channels)	58.7, 3.9, 13.1
Di-boson (WW, WZ and ZZ)	46.2, 18.0, 5.6

3.2 Background processes

The following processes are backgrounds to the $A/H/h \to \tau^+\tau^-$ signal in the lepton-hadron channel and have been considered in this analysis:

- $W(\to \ell\nu)$+jets production: W + jets production provides a significant source of background due to its relatively large cross section and the combination of a charged lepton and missing transverse energy from a leptonic decay of the W boson in the final state. Hadronic jets accompanying the W boson can be misidentified as hadronic τ decays.

- $Z/\gamma^*(\to \ell^+\ell^-)$+jets production: With a di-τ final state and similar event kinematics, $Z \to \tau^+\tau^-$ decays and Drell-Yan events $q\bar{q} \to \gamma^* \to \tau^+\tau^-$ are largely irreducible and therefore provide a significant source of background. They are particularly important for low Higgs boson masses where the signal falls on the tail of the Z mass peak in the $\tau^+\tau^-$ visible mass distribution. $Z \to e^+e^-$ and $Z \to \mu^+\mu^-$ decays and Drell-Yan events with electron or muon pairs also contribute if one of the charged leptons or an accompanying hadronic jet is misidentified as τ lepton.

- Di-boson production: The electroweak production of pairs of vector bosons (WW, WZ, ZZ) can lead to final states with two or more charged leptons from the leptonic decays of the W and Z bosons.

- QCD jet processes: Because of the large cross sections for QCD di-jet or multi-jet processes, they provide an important background if one of the jets is misidentified as a hadronic τ decay and another jet as an electron or muon.

- $t\bar{t}$ production: Due to the decays of the two t quarks ($t\bar{t} \to W^+bW^-\bar{b}$), this process can create real electrons, muons or τ leptons as well as missing transverse energy in the final state if the W bosons decay leptonically. In addition, the decays of B hadrons or a hadronic decay of a W boson bear a potential for misidentification as hadronic τ decays.

- Single-t production: The production of single t quarks via t or s-channel production or in association with a W boson contributes to the background if one W boson decays leptonically and the τ lepton is either due to a misidentified hadronic jet or, for Wt production, comes from the decay of the second W boson.

The production of W and Z bosons in association with jets is simulated with the ALPGEN [18] generator, which uses MLM matching [19] between the hard process, calculated with leading-order matrix elements for up to 5 jets, and parton showers. The $t\bar{t}$, single-t (t/s-channels, Wt) and electroweak di-boson (WW, WZ, ZZ) production processes are generated with MC@NLO. For all event samples described above, parton showers and hadronization are simulated with HERWIG [20] and the activity of the underlying event with JIMMY [21]. The loop-induced $gg \to WW$ processes are generated using gg2WW [22]. QCD jet production is generated with PYTHIA [23]. The following parton distribution function sets are used: CTEQ6.6 [24] for MC@NLO, CTEQ6L1 [25] for ALPGEN and SHERPA and modified leading-order MRST2007 [26] for PYTHIA samples. The programs TAUOLA [27] and PHOTOS [28] are used to model the decay of τ leptons and additional photon radiation from charged leptons in the leading-log approximation, respectively. The cross sections for the above processes used in this analysis are summarized in Table 1, except for the QCD jet samples which are normalized to data as described in Section 5. All simulated samples include pile-up produced with the default ATLAS MC10 tunes [29, 30] and are passed through a full simulation of the ATLAS detector based on GEANT4 [31, 32]. The simulated events are reweighted so that the distribution of the number of vertices per bunch crossing matches the data.

3.3 Data Sample

The results presented in this note are based on proton-proton collision data collected with the ATLAS experiment at the LHC at a center-of-mass energy of $\sqrt{s} = 7$ TeV. The integrated luminosity of the data sample, considering only data-taking periods where all subsystems of the ATLAS detector relevant for this analysis were fully operational, corresponds to (36.1 ± 1.2) pb^{-1} [8].

4 Object reconstruction and trigger

In this section, the reconstruction and identification of the objects relevant for the MSSM Higgs search, namely electrons, muons, hadronic τ decays and jets, are discussed. Also the reconstruction of the missing transverse energy in the event and the trigger requirements used in this analysis are presented.

4.1 Electrons

Electron candidates are reconstructed from a cluster of energy deposits in the electromagnetic calorimeter that is matched to a track in the inner detector. For electron identification, also the shower shape in the calorimenter is used [33]. Electrons are required to have a transverse momentum above 20 GeV and to be in the fiducial volume of the detector barrel or endcaps, $1.52 < |\eta| < 2.47$ or $|\eta| < 1.32$. Identified electrons are required to be isolated. The additional transverse energy in the electromagnetic and hadronic calorimeters in a cone of radius $\Delta R = 0.3$ around the electron direction must be less than 10% of the electron transverse energy. The radius ΔR is defined by $\Delta R = \sqrt{(\Delta\eta)^2 + (\Delta\phi)^2}$, where $\Delta\eta$ and $\Delta\phi$ are the differences in pseudorapidity and azimuthal angle, respectively. The transverse momentum sum of all tracks within a cone of radius $\Delta R = 0.4$ around the electron direction and with transverse momenta above 1 GeV must be less than 6% of the electron track transverse momentum.

4.2 Muons

Muon candidates are reconstructed by combining tracks in the muon spectrometer with tracks in the inner detector [33]. Muon candidates are required to have a transverse momentum above 10 GeV and a pseudorapidity $|\eta| < 2.5$. In addition, muons are required to be isolated. For isolation, the calorimeter transverse energy in a cone of radius $\Delta R = 0.4$ around the muon direction must be less than 6% of the muon transverse momentum. In addition, track isolation requirements are applied. The transverse momentum sum of all tracks within a cone of radius $\Delta R = 0.4$ around the muon direction and with transverse momenta above 1 GeV must be less than 6% of the muon track transverse momentum.

4.3 Hadronic τ decays

Candidates for hadronic τ decays are reconstructed with an algorithm that uses clusters in the electromagnetic and hadronic calorimeters as seeds. Candidates must have a transverse momentum above 20 GeV and a pseudorapidity $|\eta| < 2.5$. The number of charged tracks associated with the τ candidate must be 1 or 3 and a τ-candidate charge of ± 1, determined from the associated track(s), is required. It has been checked with simulated signal events that the charge misidentification probability for 1-prong and 3-prong τ candidates that have been geometrically matched to generated τ leptons amounts to significantly less than 1% in both cases. The identification of hadronic τ decays, including vetoes against electrons and muons, is based on observables that describe the shape of the calorimeter shower and on tracking information, which are combined in a likelihood discriminator [34]. For the τ identification used in this analysis, the efficiency for $p_T^{\tau,vis} > 20$ GeV is about 65% (60%) and the probability to misidentify a jet as tau lepton, determined from a di-jet control sample, is about 10% (5%) for 1-prong (3-prong) tau decays.

4.4 Jets

Hadronic jets are reconstructed with the anti-k_T algorithm [35, 36, 37], an infrared and collinear-safe jet clustering algorithm, with distance parameter $\Delta R = 0.4$. The jet algorithm is run on topological clusters [38] in the calorimeters. A simple p_{T}- and η-dependent calibration scheme based on Monte Carlo simulation is used to convert the electromagnetic calibration of the ATLAS calorimeters to the calibrated hadronic scale [39]. The energies of the calorimeter clusters are also corrected for losses due to dead material and out-of-cluster losses [40].

Jets are required to have transverse momenta above 20 GeV and pseudorapidities $|\eta| < 4.5$. They are not explicitly used in the event selection but are needed to estimate the systematic uncertainty of the missing-transverse-energy reconstruction due to the uncertainty on the jet energy scale (Section 7).

When candidates fulfilling the above criteria overlap with each other geometrically ($\Delta R < 0.2$), only one of them is selected. The overlap is resolved by selecting muons, electrons, taus and then jets in this order of priority.

4.5 Missing transverse energy

The reconstruction of the missing transverse energy is based on the energy deposited in the calorimeters in all cells in the region $|\eta| < 4.5$. A cell-based algorithm is used which handles the calorimeter response in the same way as it is done for jets. The sum of the transverse momenta of all reconstructed muons in the event is added to the total transverse momentum vector from the calorimeter information [41].

4.6 Trigger

An electron or muon trigger is used to trigger the events in the electron and muon channels, respectively. Events in the electron channel are selected by triggering on a cluster in the electromagnetic calorimeter and associated track with $E_{\mathrm{T}} > 10 - 15$ GeV. Events in the muon channel are triggered by a muon candidate with $p_{\mathrm{T}} > 10 - 13$ GeV. Only unprescaled triggers are used and the trigger thresholds are adjusted for the different data-taking periods according to the instantaneous luminosity of the LHC. The total trigger efficiencies are 99% and 82% for electrons and muons, respectively. They are well modeled by simulation and have an uncertainty of $0.5 - 1\%$.

5 Event Selection

Collision events that pass the trigger conditions discussed in Section 4.6 are selected if they have a vertex formed by at least three tracks. To reduce non-collision events, e.g. cosmic or beam-halo events, the reconstructed vertex position along the beam axis must be within 15 cm of the nominal vertex position. Several quality criteria are applied to suppress sources of fake missing transverse energy [42], such as poorly reconstructed jets or electrons with mis-measured energy due to inefficient regions of the LAr calorimeter.

The signatures of $A/H/h \to \tau^+\tau^-$ signal events, where one τ lepton decays leptonically, the other hadronically, are an isolated electron or muon, a narrow jet from the hadronic τ decay and missing transverse energy due to the undetected neutrinos from the two τ decays. The following requirements using the objects defined in Section 4 are imposed:

- $N_e + N_\mu = 1$, $p_{\mathrm{T}}^e > 20$ GeV or $p_{\mathrm{T}}^\mu > 15$ GeV: Exactly one electron or muon is required with transverse momentum above 20 GeV or 15 GeV, respectively. Events with more than one electron/muon, using the lepton p_{T} threshold used in the object definition in Section 4, are rejected to suppress events from $Z \to e^+e^-$ and $Z \to \mu^+\mu^-$ decays and from $t\bar{t}$ and single-t production.

- $N_\tau = 1$, $p_{\mathrm{T}}^{\tau,vis} > 20$ GeV: Exactly one identified hadronically decaying τ candidate with visible transverse momentum above 20 GeV is required.

- $Q_\tau \cdot Q_{e/\mu} = -1$: Since neutral Higgs bosons decay into a pair of oppositely-charged τ leptons the charge $Q_{e/\mu}$ of the electron/muon and Q_τ, the total charge of the hadronic τ decay products, must have opposite signs.

- $E_{\mathrm{T}}^{\mathrm{miss}} > 20$ GeV: The missing transverse energy requirement rejects events with jets from QCD processes as well as $Z \to e^+e^-$ and $Z \to \mu^+\mu^-$ decays, for which no significant missing transverse energy is expected.

- $M_{\mathrm{T}} < 30$ GeV: The transverse mass, M_{T}, of the lepton and the missing transverse energy is defined as

$$M_{\mathrm{T}} = \sqrt{2 p_{\mathrm{T}}^{\mathrm{e}/\mu} E_{\mathrm{T}}^{\mathrm{miss}} (1 - \cos\Delta\phi)}, \tag{1}$$

  where $p_{\mathrm{T}}^{\mathrm{e}/\mu}$ is the transverse momentum of the electron/muon and $\Delta\phi$ is the angle between the electron/muon and the $E_{\mathrm{T}}^{\mathrm{miss}}$ vector in the plane perpendicular to the beam direction. The requirement of low M_{T} reduces background contributions from W + jets and $t\bar{t}$ production with a real W boson in the final state which lead to M_{T} values around the W mass.

No requirements are imposed on the number of identified b-quark jets or the total number of jets in the event to keep the analysis as inclusive as possible.

After the full selection, the signal efficiency is 3% for $m_A = 120$ GeV and 8% for $m_A = 200$ GeV (not including the Higgs and τ branching ratios). Table 2 summarizes the numbers of events that pass each selection requirement, for the electron and muon channel separately. Here, the expected numbers of signal and background events from simulation are normalized according to the theoretical cross-section predictions in Table 1, except for the QCD jet sample for which the normalization is derived from data in a region of $E_{\mathrm{T}}^{\mathrm{miss}} < 15$ GeV after the $N_\tau = 1$ requirement has been applied. After the full selection, a total number of 74 and 132 events are observed in data in the electron and muon channel, respectively. No significant deviations between the observed and expected event yields are observed.

Due to the large statistical uncertainties of some of the simulated samples, especially for the QCD jet background, a reasonable comparison between data and expected background distributions is only possible after an estimation of some of the backgrounds based on data control samples.

After the selection described in this section, the invariant mass of the visible decay products of both τ decays, i.e., the electron or muon from the leptonic τ decay and the hadron(s) from the hadronic τ decay, $M_{\tau\tau}^{\mathrm{visible}}$ ("visible mass"), is used as the discriminating variable to search for a potential Higgs signal.

6 Background Estimation

It is desirable to estimate the background contributions as much as possible from data control samples to reduce the dependence on Monte Carlo simulations. The goal is to obtain the normalization and shape of the $M_{\tau\tau}^{\mathrm{visible}}$ distribution used as discriminating observable in the Higgs search for the sum of all background contributions. The most relevant background sources to be determined with data are W + jets, Z + jets, and QCD jet production, and methods for estimating these backgrounds have been developed in this analysis. First the data-driven $Z \to \tau^+\tau^-$ background estimation method is presented, then two methods to estimate the QCD and W + jets backgrounds are discussed; one is used to obtain the results of this analysis, the other as a cross-check. The remaining backgrounds from $t\bar{t}$, single-t, $Z \to \ell^+\ell^-$ ($\ell = e, \mu$) and electroweak di-boson production make up less than 5% of the total background and are estimated solely from simulation.

Table 2: Selected number of events in data and expected from simulation for a data sample corresponding to 36 pb^{-1}. Only the Monte Carlo (MC) statistical errrors are quoted.

	Electron channel		
	$N_\tau = 1$	$E_{\mathrm{T}}^{\mathrm{miss}} > 20$ GeV	$M_{\mathrm{T}} < 30$ GeV
Observed data	1413	581	74
Total MC expectation (w/o QCD)	1350±10	700±10	70±3
W+jets	710±10	590±10	26±2
Di-boson	3.61±0.05	2.68±0.05	0.26±0.01
Single-t	4.4±0.1	3.9±0.1	0.40±0.06
$t\bar{t}$	26.3±0.4	23.8±0.4	2.8±0.1
$Z/\gamma^* \to e^+e^-, \mu^+\mu^-$	451±7	41±2	9.8±0.9
$Z/\gamma^* \to \tau^+\tau^-$	150±4	40±2	30±2
$A/H/h$ signal (m_A = 120 GeV, $\tan\beta$ =40)	62±1	23.4±0.6	17.9±0.5
$A/H/h$ signal (m_A = 200 GeV, $\tan\beta$ =40)	16.4±0.2	9.7±0.2	7.3±0.2
	Muon channel		
	$N_\tau = 1$	$E_{\mathrm{T}}^{\mathrm{miss}} > 20$ GeV	$M_{\mathrm{T}} < 30$ GeV
Observed data	1627	841	132
Total MC expectation (w/o QCD)	1680±20	1050±10	137±4
W+jets	1030±10	860±10	41±2
Di-boson	4.88±0.07	3.93±0.06	0.42±0.02
Single-t	5.7±0.1	5.1±0.1	0.65±0.05
$t\bar{t}$	33.2±0.4	30.0±0.4	3.9±0.1
$Z/\gamma^* \to e^+e^-, \mu^+\mu^-$	253±5	48±2	11±1
$Z/\gamma^* \to \tau^+\tau^-$	350±20	97±3	81±3
$A/H/h$ signal (m_A = 120 GeV, $\tan\beta$ = 40)	103±1	42.9±0.9	35.4±0.8
$A/H/h$ signal (m_A = 200 GeV, $\tan\beta$ = 40)	23.8±0.3	14.6±0.2	11.4±0.2

6.1 Estimation of Z + jets background

The shape of the $M_{\tau\tau}^{\text{visible}}$ distribution from the irreducible $Z \to \tau^+\tau^-$ background, in particular the tail towards larger $M_{\tau\tau}^{\text{visible}}$ values, has been determined with a data-driven method based on a so-called embedding technique. This method starts from a high-purity $Z \to \mu^+\mu^-$ sample selected in data. The muons in these events are subsequently replaced by simulated τ leptons according to the following procedure:

- muon tracks and associated calorimeter cells are removed from the event;
- a mini event containing only two τ leptons that replace the two muons and whose decays are generated by TAUOLA [27] is passed through the ATLAS detector simulation;
- the original data event, from which the muons have been removed, and the simulated mini event are combined and a full reconstruction of the resulting new event is performed.

Thus, only the τ decays and the corresponding detector response are taken from simulation while the underlying Z kinematics and all other properties of the event are obtained from the $Z \to \mu^+\mu^-$ data.

The performance of the embedding is illustrated in Fig. 1. The distributions of the transverse mass and the visible mass are compared between $Z \to \tau^+\tau^-$ simulation and the event sample obtained from the embedding procedure applied to the whole data set corresponding to 36 pb^{-1}. For a statistically more significant comparison, the plots are not only shown after the full selection (Section 5) but also for a looser selection without M_{T} and $E_{\text{T}}^{\text{miss}}$ requirements. A good agreement between the simulated $Z \to \tau^+\tau^-$ sample and the τ-embedded $Z \to \mu^+\mu^-$ data sample is observed. Since it could be shown that the $Z \to \tau^+\tau^-$ simulation reproduces the data well, the estimate of the $Z \to \tau^+\tau^-$ background in this analysis is taken from simulation and is normalized according to the theoretical cross sections given in Table 1.

6.2 Estimation of QCD and W + jets background

The estimation of the QCD and W + jets backgrounds [43] is based on both ATLAS data and simulation and uses events with same-sign charges of the electron/muon and the hadronically decaying τ candidate. It relies on the assumptions that the shape of the $M_{\tau\tau}^{\text{visible}}$ distribution for these backgrounds is the same for opposite-sign (OS) and same-sign (SS) events and that their ratio is the same in the signal region, defined by the nominal selection described in Section 5, and in background-enhanced control regions. These assumptions have been verified with simulated events; the OS/SS ratios and the shapes of the $M_{\tau\tau}^{\text{visible}}$ distributions for opposite-sign and same-sign events agree within statistical uncertainties for both QCD and W + jets backgrounds. Two control regions are defined, a QCD-dominated control region at small $E_{\text{T}}^{\text{miss}}$ and with a relaxed isolation for the electron/muon, and a W-dominated control region at large M_{T}.

The total number of estimated opposite-sign background events in the signal region, $n_{\text{OS}}^{Bkg}(m_{\text{vis}})$, in each bin of the $M_{\tau\tau}^{\text{visible}}$ distribution can be expressed as

$$n_{\text{OS}}^{Bkg}(m_{\text{vis}}) = r_{\text{QCD}} \cdot n_{\text{SS}}^{\text{QCD}}(m_{\text{vis}}) + r_{W+\text{jets}} \cdot n_{\text{SS}}^{W+\text{jets}}(m_{\text{vis}}) + n_{\text{OS}}^{Z+\text{jets}}(m_{\text{vis}}) + n_{\text{OS}}^{\text{other}}(m_{\text{vis}}), \tag{2}$$

where r_{QCD} and $r_{W+\text{jets}}$ are the ratios of opposite-sign and same-sign events and $n_{\text{SS}}^{\text{QCD}}(m_{\text{vis}})$ and $n_{\text{SS}}^{W+\text{jets}}(m_{\text{vis}})$ are the numbers of same-sign events in the signal region for the QCD and W + jets backgrounds; $n_{\text{OS}}^{Z+\text{jets}}(m_{\text{vis}})$ and $n_{\text{OS}}^{\text{other}}(m_{\text{vis}})$ are the numbers of opposite-sign events in the signal region for $Z \to \tau^+\tau^-$ and the remaining background denoted by "other" (i.e., the sum of all backgrounds apart from $Z \to \tau^+\tau^-$, W + jets and QCD jet production).

The ratio r_{QCD} is expected to be rather close to unity. The fact that the charges of the electron/muon candidate and the τ candidate from a misidentified jet in QCD processes are approximately uncorrelated is more evident for gluon-initiated jets than for quark-initiated jets. However, since the jet momenta

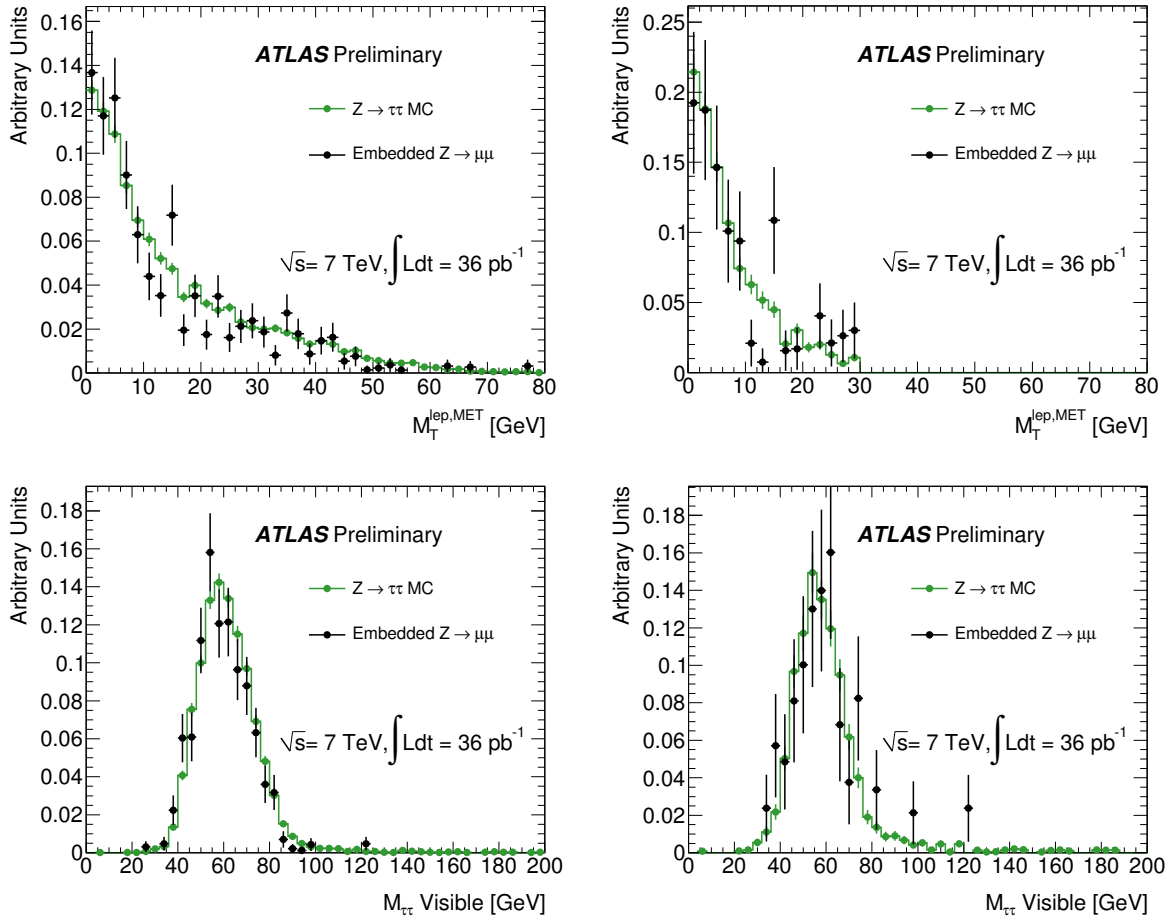

Figure 1: Comparison of the transverse mass (top) and visible mass (bottom) distributions for $Z \to \tau\tau$ simulation and the τ-embedded $Z \to \mu^+\mu^-$ sample at two stages of the selection: prior to the $E_{\mathrm{T}}^{\mathrm{miss}}$ requirement (left) and after the full event selection (right).

in this analysis are relatively moderate, the jets are expected to be mostly due to gluons. For $r_{W+\text{jets}}$ a significant deviation from unity is expected since W + jets production is dominated by gu/gd-processes that often give rise to a jet originating from a quark whose charge is anti-correlated with the charge of the W boson. From simulation, the following OS/SS ratios are obtained: $r_{\text{QCD}} = 1.06 \pm 0.13$ and $r_{W+\text{jets}} = 2.24 \pm 0.13$.

Using the deviation of the OS/SS ratio for W + jets from unity, $k_{W+\text{jets}} = r_{W+\text{jets}} - 1$, and assuming $r_{\text{QCD}} = 1$, Eq. 2 can be written as

$$n_{\text{OS}}^{Bkg}(m_{\text{vis}}) = n_{\text{SS}}^{Bkg}(m_{\text{vis}}) + k_{W+\text{jets}} \cdot n_{\text{SS}}^{W+\text{jets}}(m_{\text{vis}}) + n_{\text{OS}}^{Z+\text{jets}}(m_{\text{vis}}) - n_{\text{SS}}^{Z+\text{jets}}(m_{\text{vis}}) + n_{\text{OS}}^{\text{other}}(m_{\text{vis}}) - n_{\text{SS}}^{\text{other}}(m_{\text{vis}}), \quad (3)$$

where $n_{\text{SS}}^{Bkg}(m_{\text{vis}})$ is the sum of all same-sign backgrounds in the signal region. Each of the terms in Eq. 3 is estimated separately and for each bin in the $M_{\tau\tau}^{\text{visible}}$ distribution, thus not only an estimation of the background normalization but also of the $M_{\tau\tau}^{\text{visible}}$ shape is obtained. The opposite- and same-sign contributions from the $Z \to \tau^+\tau^-$,$n_{\text{OS}}^{Z+\text{jets}}(m_{\text{vis}})$ and $n_{\text{SS}}^{Z+\text{jets}}(m_{\text{vis}})$, and the other backgrounds, $n_{\text{OS}}^{\text{other}}(m_{\text{vis}})$ and $n_{\text{SS}}^{\text{other}}(m_{\text{vis}})$, are taken from simulation. The remaining terms in Eq. 3 are related to the W + jets and QCD backgrounds and are determined as follows:

- **Determination of n_{SS}^{Bkg}:** The total number of same-sign events n_{SS}^{Bkg} is determined for the selection described in Section 5 except for changing the opposite-sign charge requirement to same-sign. In the full $M_{\tau\tau}^{\text{visible}}$ range, a total of 36 same-sign events are selected in data.

- **Verification of the consistency of r_{QCD} with unity:** To check the assumption $r_{\text{QCD}} \approx 1$, a data control region is selected which is dominated by relatively low-E_{T} jets from QCD processes, as expected for the signal region. This is achieved by replacing the requirement $E_{\text{T}}^{\text{miss}} > 20$ GeV with $E_{\text{T}}^{\text{miss}} < 15$ GeV and by relaxing the isolation requirement for the electron/muon candidate. The contribution from other backgrounds is estimated from simulation and subtracted. A value of $r_{\text{QCD}} = 1.16 \pm 0.04 \pm 0.09$ is obtained, where the first error is due to the statistical uncertainty of the events in the $E_{\text{T}}^{\text{miss}} < 15$ GeV control region and the second error is systematic. All systematic uncertainties described in Section 7 have been propagated to the error of r_{QCD}. Since the method described in Eq. 3 assumes $r_{\text{QCD}} = 1$, but the measured central value is larger than one, the error on r_{QCD} is increased by an additional systematic uncertainty of 0.16, corresponding to the observed deviation from unity, and propagated to the error on the estimated number of background events in the signal region. The observed slight deviation of r_{QCD} from unity does not have a significant effect on the results of the background-estimation method since the QCD background contribution is very small, as discussed in Section 6.3. It has been verified with simulated QCD jet events that the value of r_{QCD} is approximately the same in the control and the signal regions.

- **Determination of $k_{W+\text{jets}}$ and $n_{\text{SS}}^{W+\text{jets}}$:** The quantity $k_{W+\text{jets}} = r_{W+\text{jets}} - 1$ is determined in a W + jets-dominated data control region which is obtained by requiring $M_{\text{T}} > 50$ GeV. The contribution from backgrounds other than W + jets is subtracted based on simulation. A value of $k_{W+\text{jets}} = 1.43 \pm 0.15$ is determined, where the error is statistical. It has been checked with simulated W+jets events that this ratio is independent of the M_{T} range considered and stays constant as a function of $M_{\tau\tau}^{\text{visible}}$ within uncertainties. The measured value of $k_{W+\text{jets}}$ is consistent with the one obtained from simulation and is assumed to be the same in the W + jets control region and the signal region. The number of same-sign W + jets events, $n_{\text{SS}}^{W+\text{jets}}$, after the full selection is determined from the number of events in the W+jets control region after subtraction of the other backgrounds based on simulation. The difference in W + jets event yields between the nominal selection with $M_{\text{T}} < 30$ GeV and the one with the $M_{\text{T}} > 50$ GeV requirement is corrected for with a correction factor obtained from simulation. The resulting number of W+jets events is $k_{W+\text{jets}} \cdot n_{\text{SS}}^{W+\text{jets}} = 31 \pm 5$, where the error contains both statistical and systematic errors. In the current study, the shape of this

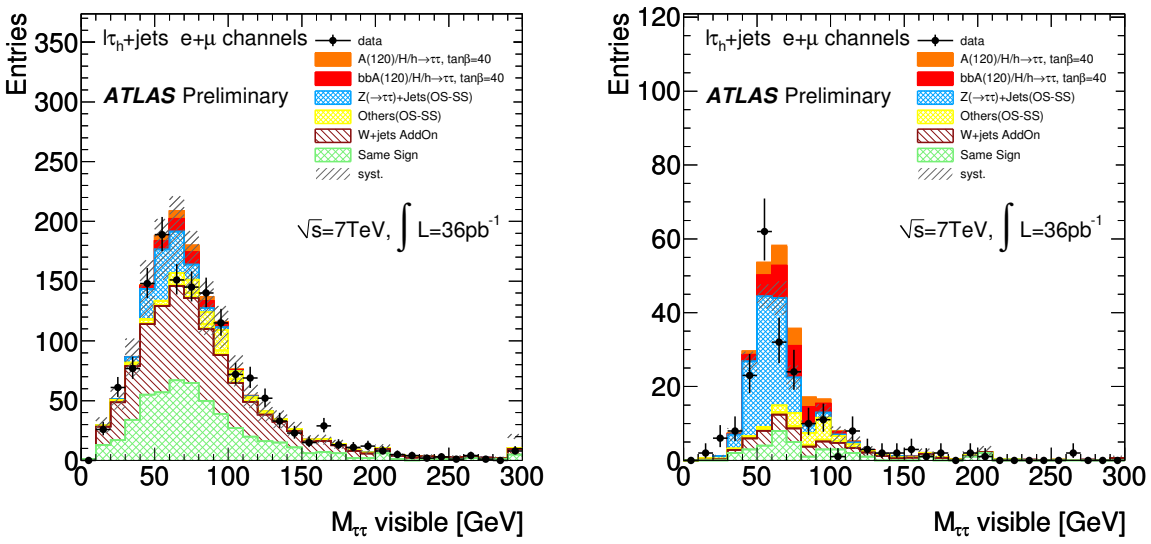

Figure 2: Visible mass distribution for data and the data-driven background estimate for the selection without a requirement on M_{T} (left) and the full selection (right). The last bin is used as overflow bin for all events with $M_{\tau\tau}^{\mathrm{visible}} > 290$ GeV.

contribution, referred to as "W + jets add-on", is taken from the $M_{\tau\tau}^{\mathrm{visible}}$ distribution for opposite-sign events, after subtracting that from same-sign events in W+jets simulation. It has been verified in simulation that the shape of the $M_{\tau\tau}^{\mathrm{visible}}$ distribution is the same for opposite-sign and same-sign events.

The estimated values for n_{SS}^{Bkg}, $k_{W+\mathrm{jets}} \cdot n_{\mathrm{SS}}^{W+\mathrm{jets}}$ and the numbers of same-sign and opposite-sign events for $Z \rightarrow \tau^+\tau^-$ ($n_{\mathrm{OS}}^{Z+\mathrm{jets}}(m_{\mathrm{vis}}) - n_{\mathrm{SS}}^{Z+\mathrm{jets}}(m_{\mathrm{vis}}) = 105 \pm 32$) and for the other backgrounds ($n_{\mathrm{OS}}^{\mathrm{other}}(m_{\mathrm{vis}}) - n_{\mathrm{SS}}^{\mathrm{other}}(m_{\mathrm{vis}}) = 24 \pm 5$) from simulation yield a total of $n_{\mathrm{OS}}^{Bkg} = 195 \pm 33$ background events which agrees well with the observation of 206 events in data for the full selection. The quoted errors on n_{OS}^{Bkg} include all statistical and systematic uncertainties. The systematic uncertainties associated with this method are discussed in Section 7. Figure 2 shows the visible mass distribution for the full selection (right) and for a looser selection without the requirement on M_{T} (left). For the looser selection, the distributions of some of the variables used in the selection are shown in Fig. 3. The shapes of the data distribution and the total background distribution obtained from the background estimation method are in good agreement. The method discussed in this section serves as the default method for the estimation of backgrounds to derive the results of this analysis.

6.3 Alternative QCD and W + jets background estimation

A second data-driven QCD and W + jets background estimation method has been developed to cross-check the results obtained from the method described in Section 6.2. While the latter method estimates the QCD and W + jets backgrounds simultaneously, this method provides a separate estimate of the QCD and W + jets backgrounds from data.

The shape of the W + jets background is taken from simulation and its normalization is derived from a W-dominated data control sample obtained by replacing the $M_{\mathrm{T}} < 30$ GeV requirement in the nominal selection by $70 < M_{\mathrm{T}} < 120$ GeV. The estimated W + jets background after the full selection amounts to 58.5 ± 2.3 events.

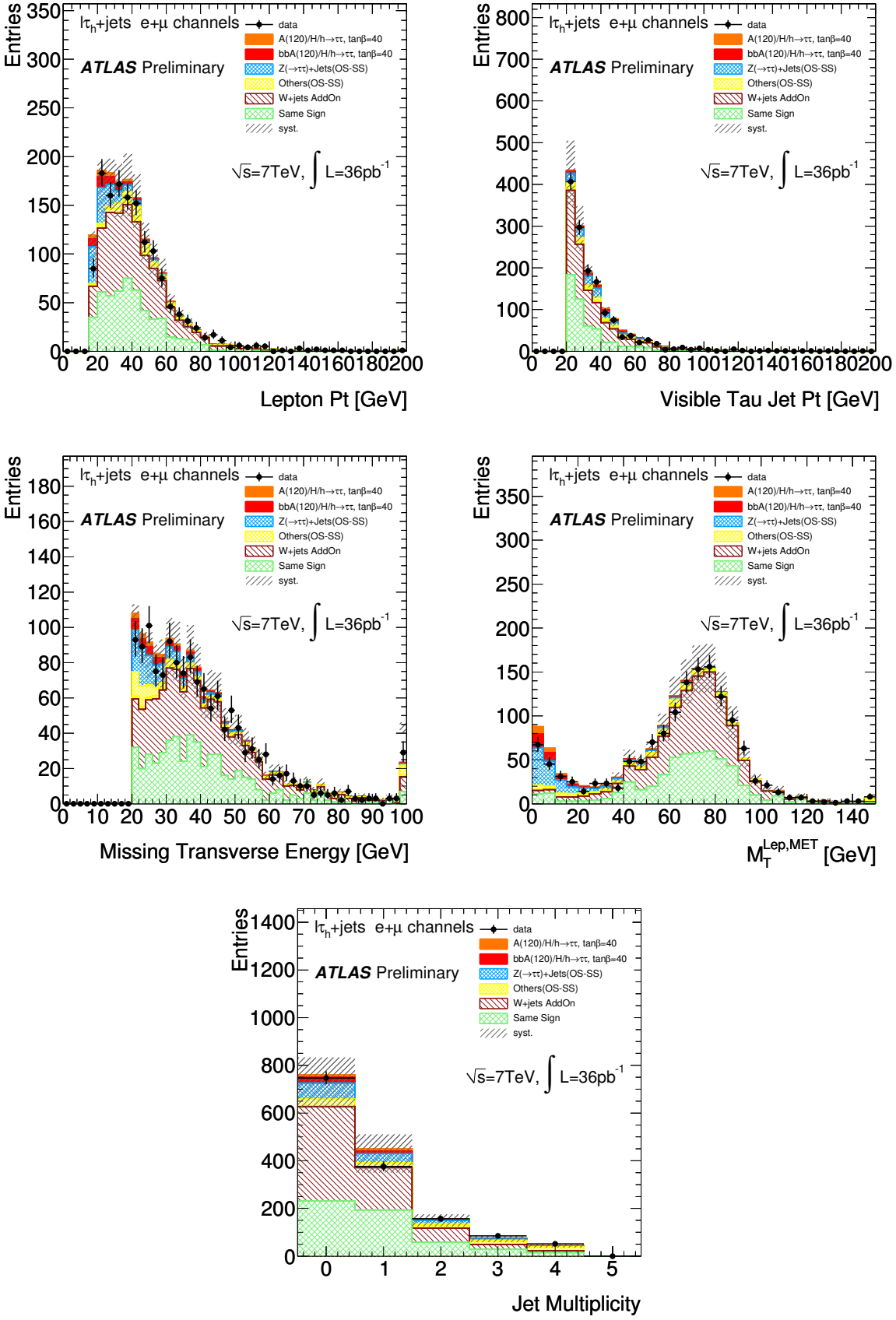

Figure 3: Distributions of selection variables and of the number of jets in the event (jet multipicity) for data and the data-driven background estimate for the selection without a requirement on M_{T}.

For the estimation of the QCD background, selection criteria on two variables, the isolation of the electron/muon and the charge product of the electron/muon and the τ candidate, are used to define four independent event samples, corresponding to four regions in the plane of the two variables. One of these four regions, the signal region, contains the events that pass the nominal event selection. The other three are control regions that are dominated by QCD background. Table 3 illustrates the definition of the four regions.

Table 3: Definition of signal and control regions for the alternative QCD background estimation method, defined by two variables: the charge product of the electron/muon and the τ candidate (OS or SS) and the isolation of the electron/muon (isolation or inverted isolation).

	Isolation	Inverted Isolation
OS	Signal region A	Control region B
SS	Control region C	Conrol region D

The shape of the visible mass distribution in control region C (same-sign events) is used as an estimate for the shape of the QCD background in the signal region A. To obtain the correct normalization for the signal region, this distribution is scaled by the ratio of events in control regions B and D. This method relies on two assumptions:

- the two variables used to define the four regions are uncorrelated;
- the selected QCD-dominated control samples contain, to a good approximation, no signal events.

Table 4 shows the number of observed data events and the expected numbers of events for the various signal and background processes for all four regions. The signal contribution in the control regions B, C and D is negligible for all m_A values considered. While the control regions B and D are clearly dominated by QCD events, region C contains a significant fraction of other backgrounds; these backgrounds are subtracted using the estimate for W + jets discussed above, and Z + jets and the other backgrounds from simulation.

Due to the stringent electron and muon isolation criteria used in this analysis only 33 data events are seen in control region C. The ratio of the number of data events in regions B and D is $r_{B/D} = 1.14 \pm 0.05$, where the error is statistical. Using this ratio and the number of data events from region C after subtraction of non-QCD backgrounds, $n_C^{non-QCD}$, the estimated number of QCD background events in signal region A is

$$n_A^{QCD} = r_{B/D} \times (n_C^{data} - n_C^{non-QCD}) = 12.1 \pm 7.1. \quad (4)$$

To check the assumption that the two variables used in this method are uncorrelated for QCD processes, the $M_{\tau\tau}^{\text{visible}}$ distribution is compared for the data in the combined regions AB and CD and for the data in AC and BD, after subtraction of the non-QCD backgrounds and neglecting the small signal contributions. In the uncorrelated case, the distributions in the two combined regions should be the same. Figure 4 shows the results of this comparison. The shapes of the distributions agree well which supports the assumption that the two variables are to a good approximation uncorrelated.

Figure 5 shows the $M_{\tau\tau}^{\text{visible}}$ and $E_{\text{T}}^{\text{miss}}$ distributions for data compared with the ones for the total background obtained from the alternative background estimation method. A good agreement is observed. The results of this method are consistent with the ones obtained from the method discussed in Section 6.2 and thus give confidence that the backgrounds in this analysis are well understood.

Table 4: Observed data events and expected numbers of events from simulation in the four regions used in the QCD background estimation. The full event selection is applied. For the simulated signal, a value of $\tan\beta = 40$ is used. The quoted errors are statistical. The number of data events in region A selected in the alternative background estimation method differs by about 1% from the number of data events after the full selection shown in Table 2. This difference is small compared to the statistical and systematic uncertainties.

	A	B	C	D
Data	203	1372	36	1195
Signal (m_A = 120 GeV)	55.2 ± 1.0	2.2 ± 0.2	0.6 ± 0.1	0.11 ± 0.03
$W \to \ell\nu$+ jets	36.8 ± 1.8	3.0 ± 0.5	13.5 ± 1.1	0.8 ± 0.3
$W \to \tau\nu$+ jets	21.7 ± 1.4	2.8 ± 0.6	5.7 ± 0.7	0.5 ± 0.2
$Z \to \ell^+\ell^-$+ jets	18.7 ± 1.3	1.8 ± 0.4	2.4 ± 0.5	0.3 ± 0.1
$Z \to \tau^+\tau^-$+ jets	103 ± 3	4.4 ± 0.6	3.8 ± 0.6	0.2 ± 0.1
$t\bar{t}$	0.0070 ± 0.0002	0.0050 ± 0.0002	0.0020 ± 0.0001	0.0049 ± 0.0002

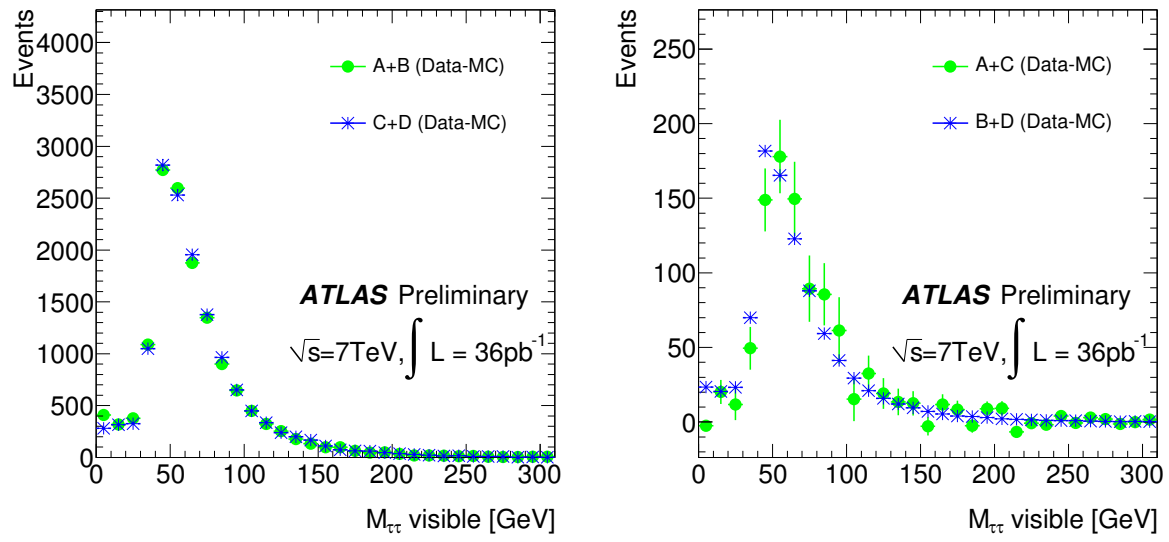

Figure 4: Comparison of the $M_{\tau\tau}^{\text{visible}}$ distributions in the combined regions AB and CD (left) and AC and BD (right) for data after subtraction of non-QCD backgrounds. The distributions are shown for the selection just before the $E_{\text{T}}^{\text{miss}}$ requirement to provide a statistically significant comparison.

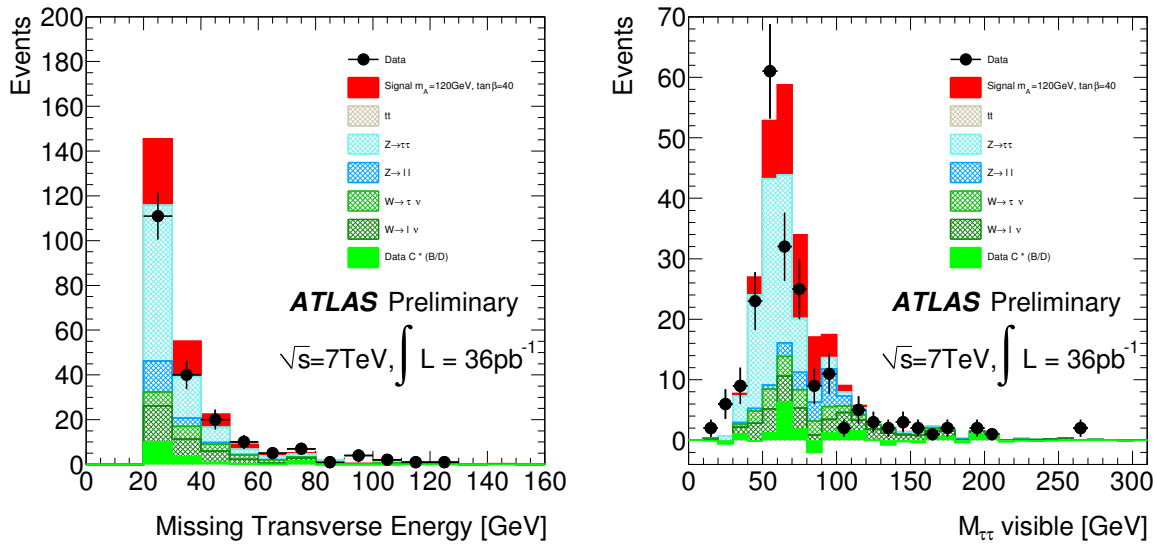

Figure 5: $E_{\mathrm{T}}^{\mathrm{miss}}$ and $M_{\tau\tau}^{\mathrm{visible}}$ distributions after the event selection for data compared with the total background obtained from the alternative background estimation method. The signal is shown for $m_A = 120$ GeV and $\tan\beta = 40$.

7 Systematic Uncertainties

The systematic uncertainties on the event yields obtained from the event selection have been evaluated. They are discussed separately for two categories, the uncertainties related to the simulation, i.e. reconstruction effects and event generation, and the uncertainties related to the data-driven background estimation.

7.1 Systematic uncertainties for simulation

For the assessment of systematic uncertainties related to the simulation, a variation of each of the sources of systematic uncertainty listed below is performed and its impact on the signal and background event yields obtained from the event selection is evaluated.

- For electrons, an uncertainty on the energy scale of $\pm 1\%$ ($\pm 3\%$) in the central (forward) detector region is used. In addition, η-dependent scale factors of $0.87 - 0.99$ with uncertainties of $3 - 6\%$ are needed to correct the electron reconstruction and identification efficiency in simulation. The relatively large deviation from unity and the sizable error are due to mismodeling of the electron isolation condition used in this analysis. The electron energy resolution is not correctly modeled in simulation, therefore a $1 - 4\%$ smearing of the constant term of the resolution is performed using a Gaussian function.

- For muons, the scale factor for the reconstruction and identification efficiency is consistent with unity and has an uncertainty of 1.8%. Since the momentum scale uncertainty is negligible, a 2% relative uncertainty is assigned as combined uncertainty for muon p_T scale and smearing and muon identification.

- Differences in trigger efficiencies between data and simulation have been corrected for with a scale factor of $(99.5 \pm 1.0)\%$ for the electron trigger and $(99.2 \pm 0.5)\%$ for the muon trigger. The uncertainties on the trigger efficiency scale factors are included as uncertainties on the event yields.

- For jets, a p_T and η-dependent uncertainty on the jet energy scale with an average of $\pm 5\%$ is used.
- For τ candidates, an uncertainty on the energy scale of $\pm 5\%$ is assumed. The τ and jet energy-scale uncertainties are treated as fully correlated. An uncertainty of 6% on the τ reconstruction and identification efficiency is used.
- The above variations applied to the individual objects are propagated to the $E_{\mathrm{T}}^{\mathrm{miss}}$ vector.

The uncertainties from the jet and τ energy scales for each simulated sample are summarized in Table 5. The largest relative uncertainty (32%) is seen for the Z + jets sample because the τ transverse momentum distribution peaks at small values around 20 GeV. The uncertainties due to electron energy scale and resolution are $0.7\% - 2.5\%$, depending on the sample. The uncertainties due to the reconstruction and identification efficiencies for electron, muons and τ candidates are approximately 8%, 2% and 4%, respectively, on all samples. Since the $Z \to e^+e^-$ background is due to misidentification of electrons as τ candidates, a 20% uncertainty is included on the misidentification rate.

No separate systematic uncertainty is assumed for $E_{\mathrm{T}}^{\mathrm{miss}}$ reconstruction. For QCD processes, where fake $E_{\mathrm{T}}^{\mathrm{miss}}$ contributions dominate and the reconstructed $E_{\mathrm{T}}^{\mathrm{miss}}$ is not well described by the simulation, the background normalization and shape is estimated purely from data. For W+jets and other backgrounds with real $E_{\mathrm{T}}^{\mathrm{miss}}$, the uncertainty on $E_{\mathrm{T}}^{\mathrm{miss}}$ is taken into account by the variation of the electron, jet and τ energy scales.

All systematic variations except for the one due to the jet and τ energy scales have a very small impact on the shape of the $M_{\tau\tau}^{\mathrm{visible}}$ distribution, therefore only changes in acceptance are considered for these error sources. The jet and τ energy scale variations have a non-negligible impact on the shape of the $M_{\tau\tau}^{\mathrm{visible}}$ distribution for signal and background. The change in the $M_{\tau\tau}^{\mathrm{visible}}$ shape that results from a variation of the jet and τ energy scales is included as additional uncertainty in the derivation of the Higgs exclusion limit in Section 8.

Uncertainties in the range of $4-13\%$ are assigned to the cross sections of background processes. The uncertainties on the signal cross sections depend on m_A and $\tan\beta$ and lie in the range of $10 - 20\%$ for both $gg \to A/H/h$ and $b\bar{b}A/H/h$ production. They include the uncertainties due to the parton distribution fuctions (PDF's) and the renormalization and factorization scales. Systematic uncertainties related to the parameters used in the event generation of background samples are evaluated by varying the relevant scale parameters, PDF choices and MLM matching conditions for the ALPGEN generator (Z + jets) and the MC@NLO generator ($t\bar{t}$).

The total uncertainty on the signal efficiency, including all reconstruction, generator and cross-section uncertainties, amounts to 24.2% and 15.4% for $m_A = 120$ GeV and $m_A = 200$ GeV, respectively. The dominant uncertainty of the signal comes from the jet and τ energy scale uncertainty.

7.2 Systematic uncertainties for background estimation from data

The systematic uncertainties for the data-driven QCD and W+jets background estimation are summarized in Table 6. The dominant sources of uncertainties are the statistical uncertainty of the same-sign events in the signal region (17%) and of the opposite-sign and same-sign events used to verify the relation $r_{\mathrm{QCD}} = 1$ (19%) in the region of $E_{\mathrm{T}}^{\mathrm{miss}} < 15$ GeV and to estimate $k_{W+\mathrm{jets}}$ (11%). Since the number of same-sign events for the "add-on contribution", $n_{\mathrm{SS}}^{W+\mathrm{jets}}$, is obtained from simulation, its statistical uncertainty is assigned as a systematic error (4%). An additional contribution of 10% is derived from the dependence of $k_{W+\mathrm{jets}}$ on M_{T}, i.e., for the extrapolation from control to signal region. Since the background estimation method is not purely based on data but also uses information from simulation, the previously discussed reconstruction and generator uncertainties need to be taken into account for the background estimation, as well as the statistical uncertainty of the simulated W+jets, Z+jets, $t\bar{t}$, single-t and di-boson samples.

Table 5: Relative systematic uncertainties on the event yields due to τ and jet energy scale variations for the signal and background samples.

	Jet/τ energy scale	
	plus	minus
$A/H/h \to \tau^+\tau^-$ (m_A = 120 GeV)	17.0%	-14.0%
$Z \to \tau^+\tau^-$+jets	31.7%	-21.0%
$Z \to e^+e^-$ or $\mu^+\mu^-$+jets	23.2%	-8.0%
$t\bar{t}$	1.0%	-1.4%
Single-t	1.3%	-1.8%
Di-boson	1.9%	0.6%

Table 6: Relative systematic uncertainties on the estimated background yields for the QCD and W + jets background estimation.

Sources	Uncertainty
Same-sign component (n_{SS}^{Bkg})	
Same-sign statistics	17%
QCD OS/SS ratio r_{QCD}	19%
Add-on component ($k_{W+\mathrm{jets}} \cdot n_{\mathrm{SS}}^{W+\mathrm{jets}}$)	
Add-on statistics $n_{\mathrm{SS}}^{W+\mathrm{jets}}$	4%
$k_{W+\mathrm{jets}}$ statistical error	11%
M_{T} dependence of $k_{W+\mathrm{jets}}$	10%
Acceptance from simulation	
Renormalization and factorization scales for $t\bar{t}$	1.7%
Scales, PDF and MLM matching scheme for Z+jets	12.5%
Electron efficiency	1.8-7.8%
Muon efficiency	2%
τ efficiency	4.1%
Electron energy scale	0.7-2.5%
Electron energy resolution	<1.2%
τ and jet energy scale	1.4-31%
Luminosity	3.4%

8 Exclusion limits

Since no excess of events above expectation is oberved, exclusion limits for the production of neutral MSSM Higgs bosons are determined as a function of the parameters m_A and $\tan\beta$. A point in the $(\tan\beta, m_A)$ plane is excluded if the signal hypothesis is rejected at the 95% confidence level. The profile likelihood method [44] is used with the visible mass as the discriminating observable. The exclusion limits are derived from a shape analysis of the $M_{\tau\tau}^{\text{visible}}$ distribution in Fig. 2 (right) obtained from the background estimation method described in Section 6.2. Systematic uncertainties are included as nuisance parameters. Two kinds of systematic uncertainties are considered, the common ones, which we assume to be fully correlated, and the channel-specific ones. The common correlated systematic uncertainties include uncertainties on the luminosity, energy scale and acceptance. Systematic uncertainties influence both the expected event yield (normalization) and the shape of the visible mass distribution. The systematic uncertainties on the shapes of the visible mass distribution due to variation of jet and τ energy scales for the backgrounds taken from simulation are included.

The likelihood, for each bin of the $M_{\tau\tau}^{\text{visible}}$ distribution, is given by

$$\mathcal{L}(\mu, \beta_{QCD}, \vec{\theta}_s, \vec{\theta}_b, \vec{\theta}_{global}) = \text{Pois}(n|\mu_T)\ \text{Pois}(n_{SS}|\beta_{QCD})\mathcal{L}(\vec{\theta}_s, \vec{\theta}_b, \vec{\theta}_{global}), \tag{5}$$

where n is the number of events in the signal region, β_{QCD} is the unknown number of QCD events in the QCD control region, measured to be n_{SS}, $\vec{\theta}_{s,b}$ are the specific nuisance parameters related to the signal and the background (such as efficiency and cross section uncertainties), $\vec{\theta}_{global}$ represent the common nuisance parameters which are correlated between channels, such as the luminosity uncertainty. μ_T is the total number of expected events given by

$$\mu_T = \sum_{l=1}^{4} \mu L \sigma_l(\tan\beta, m_A) f_s(\vec{\theta}_s) f_g(\vec{\theta}_{global}) + \sum_j L\beta_j f_b(\vec{\theta}_b) f_g(\vec{\theta}_{global}), \tag{6}$$

where L is the nominal integrated luminosity, μ is the one parameter of interest, the scaling factor for the expected signal rate (signal strength), $\sigma_l(\tan\beta, m_A)$ is the effective cross section (in pb) for signal events in channel l ($bbA/H, bbh, gg \to A/H, gg \to h$), β_j is the nominal effective cross section (in pb) for background j (including β_{QCD}) and $f_{s,b,global}$ represent the dependence of the expected number of events on the various nuisance parameters.

The likelihood is used to construct a test statistic based on the profile-likelihood ratio and asymptotic formulas [44] are used when appropriate. The test statistic is given by

$$\tilde{q}_\mu = \begin{cases} -2\ln\frac{L(\mu, \hat{\hat{\vec{\theta}}}(\mu))}{L(0, \hat{\hat{\vec{\theta}}}(0))} & \hat{\mu} < 0\ , \\ -2\ln\frac{L(\mu, \hat{\hat{\vec{\theta}}}(\mu))}{L(\hat{\mu}, \hat{\vec{\theta}})} & 0 \le \hat{\mu} \le \mu\ , \\ 0 & \hat{\mu} > \mu\ . \end{cases} \tag{7}$$

Here, $\vec{\theta}$ represent the nuisance parameters, $\hat{\mu}$, $\hat{\vec{\theta}}$, and $\hat{\hat{\vec{\theta}}}(\mu)$ are the Maximum Likelihood Estimators (MLE) of μ, $\vec{\theta}$, and the nuisance parameters evaluated at μ, repectively.

Toy MC experiments are generated to construct the PDF $f(\tilde{q}_\mu|\mu, \hat{\hat{\theta}}(\mu))$ under an assumed signal strength μ. From this, the p-value for μ is calculated using

$$p_\mu = \int_{\tilde{q}_{\mu,obs}}^{\infty} f(\tilde{q}_\mu|\mu, \hat{\hat{\theta}}(\mu))\, \mathrm{d}\tilde{\mathrm{q}}_\mu \tag{8}$$

By iteration, the value μ_{up} is found which satisfies $p_{\mu_{up}} = 5\%$. Similarly, background-only toy MC experiments are used to find the expected median μ_{med} along with the $\pm1\sigma$ and $+2\sigma$ bands. To

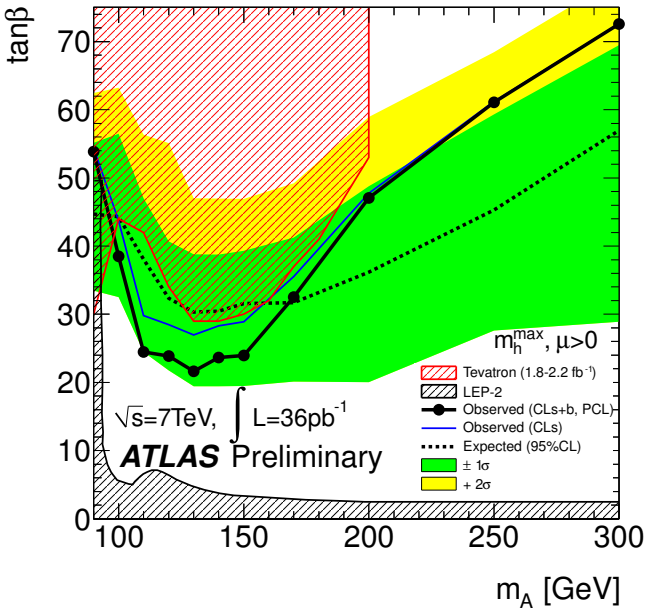

Figure 6: Expected and observed exclusion limits for neutral Higgs boson production in the MSSM as a function of m_A and $\tan\beta$ in the 4-flavor scheme. The region above the drawn limit curve is excluded at the 95% confidence level. The exclusion limits from LEP and Tevatron are also shown. For a direct comparison with the Tevatron limit, the observed limit based on CL_s is shown in addition to the one based on CL_{s+b}. The power constraint in the PCL is invoked at $m_A = 110$ GeV, where the limit is at $\tan\beta = 24$ not $\tan\beta = 22$ as it would have been without. The green and yellow bands correspond to the 1σ and 2σ error bands, respectively. The observed limit is shown up to $\tan\beta \approx 70$ while it should be noted that the region $\tan\beta > 65$ is widely considered to be theoretically not well under control.

protect against excluding the signal hypothesis in cases of downward fluctuations of the background, we do not allow the observed limit to fluctuate below the -1σ expected limit. This is equivalent to restricting the statistical power of the analysis not to go below 16%. We therefore refer to this method as power-constrained limit (PCL). If the observed limit fluctuates below the 16% power, the quoted limit is $\mu_{med} - 1\sigma$.

For each point in the parameter space $(\tan\beta, m_A)$, $\mu_{up}(\tan\beta, m_A)$ is found. If $\mu_{up}(\tan\beta, m_A) < 1$ the point $(\tan\beta, m_A)$ is excluded at the 95% CL.

Figure 6 shows the resulting exclusion limit for MSSM neutral Higgs boson production in the $\tan\beta - m_A$ plane for the m_h^{max} scenario and $\mu > 0$. The expected and observed 95% confidence-level limits are shown as solid and dashed black lines, respectively. The green and yellow bands correspond to the 1σ and 2σ error bands. The obtained limit excludes regions of parameters space beyond the existing limits from previous experiments at LEP [6] and the Tevatron [7]. It should be noted that the LEP and Tevatron limits were derived using different statistical methods.

9 Conclusions

In this note, a search for neutral MSSM Higgs bosons $A/H/h$ in proton-proton collisions at a center-of-mass energy of 7 TeV with the ATLAS experiment is presented. The study is based on a data sample that corresponds to an integrated luminosity of 36 pb^{-1}. The Higgs boson production proceeds via gluon-fusion or in association with b quarks. Candidates for Higgs decays into two τ leptons where one of

the τ leptons decays leptonically, the other hadronically are selected. A total of 206 candidate events are observed in data. The most important backgrounds to this search have been estimated with data control samples. The results of two different background-estimation methods are compared and found to be consistent with each other. The total background estimate amounts to 195 ± 33 events, in good agreement with the observed data events. Since no excess of events over the expected background is observed, exclusion limits on $A/H/h$ production are set as a function of m_A and $\tan\beta$ by using a profile-likelihood analysis of the visible $\tau^+\tau^-$ invariant mass spectrum. The obtained limits extend to regions of parameter space beyond the existing limits from other experiments.

References

[1] F. Englert and R. Brout, *Broken Symmetry and the Mass of Gauge Vector Mesons*, Phys. Rev. Lett. **13** (1964) 321.

[2] P. W. Higgs, *Broken symmetries, massless particles and gauge fields*, Phys. Lett. **12** (1964) 132.

[3] P. W. Higgs, *Broken Symmetries and the Masses of Gauge Bosons*, Phys. Rev. Lett. **13** (1964) 508.

[4] P. W. Higgs, *Spontaneous Symmetry Breakdown without Massless Bosons*, Phys. Rev. **145** (1966) 1156.

[5] L. Evans and P. Bryant, *LHC Machine*, JINST **3** (2008) S08001.

[6] S. Schael and others, LEPH Collaboration and DELPHI Collaboration and L3 Collaboration and OPAL Collaborations and LEP Working Group for Higgs Boson Searches, *Search for neutral MSSM Higgs bosons at LEP*, Eur. Phys. J. **C47** (2006) 547.

[7] The CDF Collaboration, the D0 Collaboration, the Tevatron New Physics Higgs Working Group (TEVNPHWG), *Combined CDF and D0 upper limits on MSSM Higgs boson production in $\tau - \tau$ final states with up to* 2.2 fb^{-1}, arXiv:1003.3363 [hep-ex].

[8] The ATLAS Collaboration, *Updated Luminosity Determination in pp Collisions at sqrt(s)=7 TeV using the ATLAS detector*, ATLAS-CONF-2011-011.

[9] M. Carena, S. Heinemeyer, C. E. M. Wagner, and G. Weiglein, *Suggestions for benchmark scenarios for MSSM Higgs boson searches at hadron colliders*, Eur. Phys. J. **C26** (2003) 601–607, hep-ph/0202167.

[10] The ATLAS Collaboration, G. Aad et al., *The ATLAS Experiment at the CERN Large Hadron Collider*, JINST **3** (2008) S08003.

[11] M. Spira, *HIGLU: A Program for the Calculation of the Total Higgs Production Cross Section at Hadron Colliders via Gluon Fusion including QCD Corrections*, hep-ph/9510347 (1995) .

[12] R. V. Harlander and W. B. Kilgore, *Next-to-next-to-leading order Higgs production at hadron colliders*, Phys. Rev. Lett. **88** (2002) 201801, hep-ph/0201206.

[13] LHC Higgs Cross Section Working Group, S. Dittmaier, C. Mariotti, G. Passarino, R. Tanaka (Eds.), et al., *Handbook of LHC Higgs Cross Sections: 1. Inclusive Observables*, arXiv:1101.0593 [hep-ph].

[14] S. Dittmaier, M. Kramer, 1, and M. Spira, *Higgs radiation off bottom quarks at the Tevatron and the LHC*, Phys. Rev. **D70** (2004) 074010, arXiv:hep-ph/0309204.

[15] M. Frank et al., *The Higgs Boson Masses and Mixings of the Complex MSSM in the Feynman-Diagrammatic Approach*, JHEP **0702** (2007) 047, hep-ph/0611326.

[16] S. Frixione and B. R. Webber, *Matching NLO QCD computations and parton shower simulations*, JHEP **06** (2002) 029, hep-ph/0204244.

[17] T. Gleisberg et al., *Event generation with SHERPA 1.1*, JHEP **02** (2009) 007.

[18] M. L. Mangano et al., *ALPGEN, a generator for hard multiparton processes in hadronic collisions*, JHEP **07** (2003) 001.

[19] J. Alwall et al., *Comparative study of various algorithms for the merging of parton showers and matrix elements in hadronic collisions*, Eur. Phys. J. **C53** (2008) 473, arXiv:0706.2569.

[20] G. Corcella et al., *HERWIG 6: an event generator for hadron emission reactions with interfering gluons (including supersymmetric processes)*, JHEP **01** (2001) 010.

[21] J. M. Butterworth, J. R. Forshaw, and M. H. Seymour, *Multiparton Interactions in Photoproduction at HERA*, Z. Phys. **C72** (1996) 637.

[22] T. Binoth, M. Ciccolini, N. Kauer, and M. Kramer, *Gluon-induced W-boson pair production at the LHC*, JHEP **12** (2006) 046.

[23] T. Sjostrand, S. Mrenna and P. Skands, *PYTHIA 6.4 physics and manual*, JHEP **05** (2006) 026.

[24] P. M. Nadolsky et al., *Implications of CTEQ global analysis for collider observables*, Phys. Rev. D **78** (2008) 013004.

[25] J. Pumplin, *New Generation of Parton Distributions with Uncertainties from Global QCD Analysis*, JHEP **0207** (2002) 012.

[26] A. Sherstnev and R. S. Thorne, *Parton Distributions for Leading Order Generators*, Eur. Phys. J. **C55** (2008) 553.

[27] S. Jadach, J. H. Kuhn and Z. Was, *TAUOLA - a library of Monte Carlo programs to simulate decays of polarized τ leptons*, Comput. Phys. Commun. **64** (1990) 275.

[28] E. Barberio, B. V. Eijk and Z. Was, *Photos - a universal Monte Carlo for QED radiative corrections in decays*, Comput. Phys. Commun. **66** (1991) 115.

[29] The ATLAS Collaboration, *First tuning of HERWIG/JIMMY to ATLAS data*, ATL-PHYS-PUB-2010-014.

[30] The ATLAS Collaboration, *Charged particle multiplicities in p p interactions at $\sqrt{s}$ = 0.9 and 7 TeV in a diffractive limited phase-space measured with the ATLAS detector at the LHC and new PYTHIA6 tune*, ATLAS-CONF-2010-031.

[31] The GEANT4 Collaboration, S. Agostinelli et al., *GEANT4 - a simulation toolkit*, Nucl. Instrum. Meth. **A506** (2003) 250.

[32] The ATLAS Collaboration, G. Aad et al., *The ATLAS Simulation Infrastructure*, ATLAS-SOFT-2010-01-004, submitted to Eur. Phys. J. C., arXiv:1005.4568.

[33] The ATLAS Collaboration, *Expected Performance of the ATLAS Experiment - Detector, Trigger and Physics*, CERN-OPEN-2008-020, arXiv:0901.0512.

[34] The ATLAS Collaboration, *Tau Reconstruction and Identification Performance in ATLAS*, ATLAS-CONF-2010-086.

[35] M. Cacciari, G. P. Salam and G. Soyez, *The anti-k_t jet clustering algorithm*, JHEP **04** (2008) 063.

[36] M. Cacciari and G. P. Salam Phys. Lett. B **641** (2006) 57.

[37] M. Cacciari, G. P. Salam and G. Soyez, *FastJet*, http://fastjet.fr/.

[38] W. Lampl et al., *Calorimeter Clustering Algorithms : Description and Performance*, ATL-LARG-PUB-2008-002.

[39] The ATLAS Collaboration, *Jet energy scale and its systematic uncertainty for jets produced in proton-proton collisions at $\sqrt{s}$ = 7 TeV and measured with the ATLAS detector*, ATLAS-CONF-2010-056.

[40] T. Barillari et al., *Local Hadron Calibration*, ATL-LARG-PUB-2009-001.

[41] The ATLAS Collaboration, *Measurement of the $W \to \ell\nu$ and $Z/gamma^* \to \ell\ell$ production cross sections in proton-proton collisions at $\sqrt{s}$ = 7 TeV with the ATLAS detector*, JHEP **1012** (2010) 060, arXiv:1010.2130 [hep-ex].

[42] The ATLAS Collaboration, *Data-Quality Requirements and Event Cleaning for Jets and Missing Transverse Energy Reconstruction with the ATLAS Detector in Proton-Proton Collisions at a Center-of-Mass Energy of $\sqrt{s}$ = 7 TeV*, ATLAS-CONF-2010-038.

[43] The ATLAS Collaboration, *Data-driven background estimation for the $H \to \tau^+\tau^- \to \ell h$ search at sqrt(s)=7 TeV with the ATLAS detector*, ATLAS-CONF-2010-096.

[44] G. Cowan, K. Cranmer, E. Gross and O. Vitells, *Asymptotic formulae for likelihood-based tests of new physics*, Eur. Phys. J. **C71** (2011) 1554, arXiv:1007.1727 [physics.data-an].